PHYSICAL REVIEW B **109**, 184103 (2024)

Structural phase transition and electronic properties of two-dimensional $NbOI_2$

Guitao Zhang,[1] Qian Chen,[1,*] and Jinlan Wang[1,2]

[1]*Key Laboratory of Quantum Materials and Devices of Ministry of Education, School of Physics, Southeast University, Nanjing 211189, China*
[2]*Suzhou Laboratory, Suzhou 215125, China*

(Received 14 December 2023; revised 29 March 2024; accepted 10 April 2024; published 1 May 2024)

The response to strains is a crucial issue when applying two-dimensional (2D) materials in flexible electronic devices. Utilizing first-principles calculations based on density functional theory, we systematically studied the structural phase transition in niobium oxide diiodide ($NbOI_2$) monolayer and the consequent changes in electronic and magnetic properties. The calculated Young's modulus of the monolayer $NbOI_2$ is approximately 80 $\mathrm{N\,m^{-1}}$, and the in-plane Poisson's ratio is less than 0.1. Under uniaxial strain, dissociation of Nb atom dimers occurs, leading to a magnetic phase transition from nonmagnetic to antiferromagnetic states. Moreover, the coupling pattern of magnetic moments exhibits significant anisotropy along different directions with temperature variations. The exchange couplings in two orthogonal crystal directions were analyzed and the Néel temperature was predicted using Monte Carlo simulations. Additionally, the strain also modulates the ferroelectric polarization and switching barriers. A clear physical picture was provided to explain the magnetic and electronic mechanisms in the 2D $NbOI_2$. This study shows the potential applications of such materials in future flexible microelectronic devices.

DOI: 10.1103/PhysRevB.109.184103

I. INTRODUCTION

In recent years, flexible electronic devices have attracted considerable attention in areas such as optoelectronic sensing, smart healthcare, and health monitoring [1–3]. With the trend towards miniaturization, multifunctionality, and high integration of electronic devices, two-dimensional (2D) materials such as graphene, MoS_2, etc., have entered the field of flexible devices due to their atomic-level thickness and planar integrability. Compared to traditional organic thin films, 2D materials exhibit superior properties in many aspects, such as mobility, magnetism, exciton lifetime, and superconductivity [4–9]. Moreover, the relatively simple structure of 2D materials can generally lead to significant changes in their properties under small strains. Previous studies have shown that strain can effectively modulate the electronic [10], optical [11], magnetic [12], and transport [13] properties of 2D materials. This characteristic allows flexible devices to exhibit more sensitive and precise effects in mechanical sensing, such as pressing, stretching, folding, and bending. Therefore, the search for stable 2D materials with mechanical sensitivity is of great significance for the research and application of flexible devices.

Niobium oxide diiodide ($NbOI_2$) has been predicted to be a new 2D van der Waals layered material with intrinsic in-plane ferroelectricity [14]. Recently, monolayer $NbOI_2$ has been experimentally obtained through mechanical exfoliation, demonstrating significant in-plane anisotropic electrical and optical properties [15]. Under external pressure, 2D $NbOI_2$ can achieve substantially tunable nonlinear optical responses [16,17]. Additionally, 2D $NbOI_2$ has also been reported to exhibit outstanding properties such as ultrastrong second harmonic generation [18], giant piezoelectric response [19], and anisotropic mechanical properties [20]. To further explore the potential applications in flexible devices, in this paper, we systematically investigated the monolayer $NbOI_2$ using first-principles calculations and provided insights into its mechanically sensitive structural, magnetic, and polarization properties.

II. COMPUTATIONAL METHOD

All calculations were performed on the basis of spin-polarized density functional theory implemented in the Vienna *ab initio* simulation package [21]. The exchange-correlation potential was described using general gradient approximation in the scheme of Perdew-Burke-Ernzerhof [22] with a plane-wave basis set cutoff energy of 520 eV. The van der Waals interactions were considered, and various correction methods were compared (see Table SI within the Supplemental Material, SM [23]), with the D3 correction [24] providing structures in agreement with experimental results [15,25]. For more accurate band structures, the Hyed-Scuseria-Ernzerhof (HSE06) exchange functional [26,27] was employed. Convergence thresholds for force and energy in ionic and electronic optimizations were set at 10^{-2} eV/Å and 10^{-6} eV, respectively. The magnetic anisotropy energy (MAE) was computed, considering the spin-orbit coupling (SOC) effect, to determine the easy magnetic axis [28]. To avoid interlayer interactions, a vacuum layer of more than 20 Å was introduced in the vertical plane direction. The k-point meshes [29] with separated space of $\sim$0.05 $\mathrm{Å^{-1}}$ were adopted to sample the Brillouin zone. Force constants were calculated using a $4 \times 2 \times 1$ supercell, and phonon spectra were obtained through PHONOPY code [30]. The energy barriers for structural phase transitions were calculated using the CI-NEB

---

[*] qc119@seu.edu.cn

TABLE I. The lattice constants (Å), polarization displacement (Å), and bandgap values (eV) for both bulk and monolayer $NbOI_2$.

	a	b	c	d_{Nb}	E_g
Bulk (experiment) [15,25]	3.92	7.52	15.18	0.13	1.70
Bulk (this paper)	3.91	7.54	15.40	0.13	1.72
Monolayer (this paper)	3.91	7.52		0.13	1.82

method [31]. Ferroelectric polarization was determined using the Berry phase method [32]. Utilizing the Heisenberg model [33], the Néel temperature was estimated through Monte Carlo simulation methods [34]. Young's moduli in the a (Y_a) and b (Y_b) directions were calculated by the following formulas [35], where C_{11}, C_{12}, C_{21}, C_{22} are the elastic stiffness constants,

$$Y_a = \frac{C_{11}C_{22} - C_{12}C_{21}}{C_{22}},$$
$$Y_b = \frac{C_{11}C_{22} - C_{12}C_{21}}{C_{11}}. \quad (1)$$

III. RESULTS AND DISCUSSION

The characterization experiments have confirmed that $NbOI_2$ is a typical van der Waals material with the space group $C2$, and its ground state is ferroelectric [15,19,25]. The lattice constants, polarization displacement, and bandgap of the bulk $NbOI_2$ were calculated and listed in Table I. They are consistent with the experimental values. Based on the validation of the computational method, we further calculated the corresponding parameters for the monolayer $NbOI_2$, as illustrated in Fig. 1(a). There are two Nb atoms, two O atoms, and four I atoms in the rectangular unit cell, with lattice constants $a = 3.91$ Å and $b = 7.52$ Å, and the structure belongs to the $Pmm2$ space group. Two adjacent Nb atoms undergo dimerization, and both deviate toward the O vertex in the NbO_2I_4 octahedron. The polarization displacement relative to the geometric center of the octahedron is $d_{Nb} = 0.13$ Å, resulting in a ferroelectric polarization. The lattice constants and polarization displacement of the monolayer $NbOI_2$ in Table I are close to those of the bulk structure. The phonon spectrum is calculated as shown in Fig. 1(b), and there are no imaginary frequencies in the Brillouin zone, indicating its dynamic stability.

The calculated band structure based on the HSE06 hybrid functional is shown in Fig. 1(c), the monolayer $NbOI_2$ is an indirect bandgap semiconductor with a gap of 1.82 eV. Compared to the bulk phase, the bandgap is increased due to quantum confinement effects. The conduction band minimum (CBM) at the Y point is mainly composed of Nb-$d_{xz/yz}$ orbitals, and the valence band maximum (VBM) at the X point is dominated by the Nb-d_{xy} orbital. As presented in the inset of Fig. 1(c), the Cartesian coordinate is defined with the z axis parallel to the Nb-O bonds and x/y axis in the plane of Nb-I bonds in the octahedron. In-depth analysis reveals that the distorted NbO_2I_4 octahedron leads to the lifting of degeneracy in the t_{2g} and e_g orbitals. Five Nb-d are labeled with different colors in the band structure. Among them, the red line representing the Nb-d_{xy} orbital shows further splitting. This is attributed to the relatively strong in-plane overlap of the d_{xy} orbitals of adjacent Nb atoms in the b direction. The overlap of wave functions with the same and opposite phases in the b direction, results in a significant difference in the electron distribution and energy of Nb-d_{xy} orbitals, known as the bonding state σ and the antibonding state σ^*. After losing four electrons to the surrounding O and I anions, only one valence electron remains in Nb^{4+} cation, occupying the Nb-d_{xy} band below the Fermi level (E_F). We further calculated the electron probability density distribution of these two bands at their respective Γ points, as shown in Fig. 1(d). Due to the dimerization, strong overlap occurs in the Nb-d_{xy} orbitals of adjacent Nb^{4+} cation, forming localized electron pairs, and leading to the quenching of the local magnetic moment.

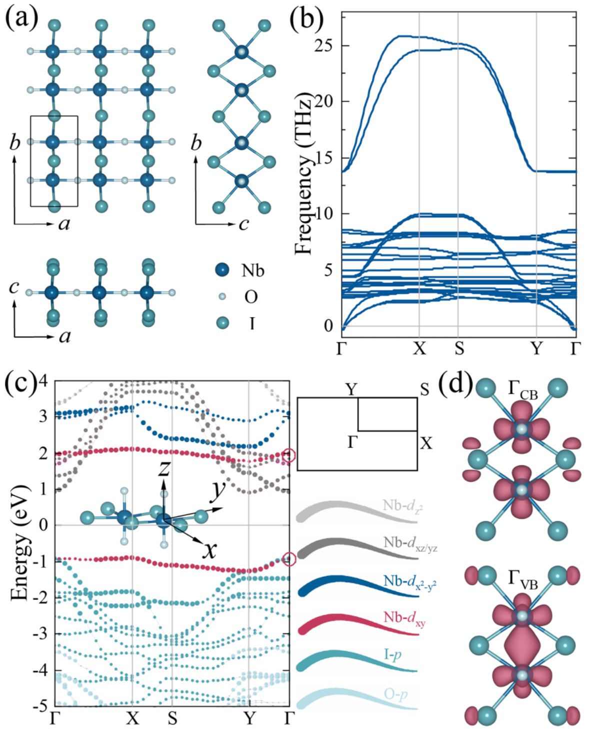

FIG. 1. (a) Atomic structure of monolayer $NbOI_2$, where the rectangular box represents the unit cell. (b) Phonon spectrum of monolayer $NbOI_2$. (c) Orbital-projected band structure calculated using the HSE06 functional, with an inset showing the Cartesian coordinates used in the band calculations. (d) The electron density plot at the Γ point in the band structure labeled by the red circle. The value of the isosurface is 0.005 e/Å^3.

By calculating the elastic constants, the mechanical properties of monolayer $NbOI_2$ were determined. Calculated values are as follows: $C_{11} = 80.4\,\mathrm{N\,m^{-1}}$, $C_{22} = 66.0\,\mathrm{N\,m^{-1}}$, $C_{12} = C_{21} = 2.7\,\mathrm{N\,m^{-1}}$, and $C_{66} = 13.7\,\mathrm{N\,m^{-1}}$. These values satisfy the mechanical stability criteria for 2D materials ($C_{11}C_{22} - C_{12}{}^2 > 0$, $C_{66} > 0$) [36]. The Young's moduli (Y_a, Y_b) along the a and b directions calculated by Eq. (1) are 80.3 $\mathrm{N\,m^{-1}}$ and 65.9 $\mathrm{N\,m^{-1}}$, respectively. These results align with previous studies [20]. The in-plane Young's moduli of monolayer $NbOI_2$ are less than those of graphene [37] ($Y_a = Y_b = 334\,\mathrm{N\,m^{-1}}$) and MoS_2 [38] ($Y_a = Y_b = 128\,\mathrm{N\,m^{-1}}$), indicating that 2D $NbOI_2$ are prone to stretching. The strain within the elastic deformation range is calculated to fit the data and

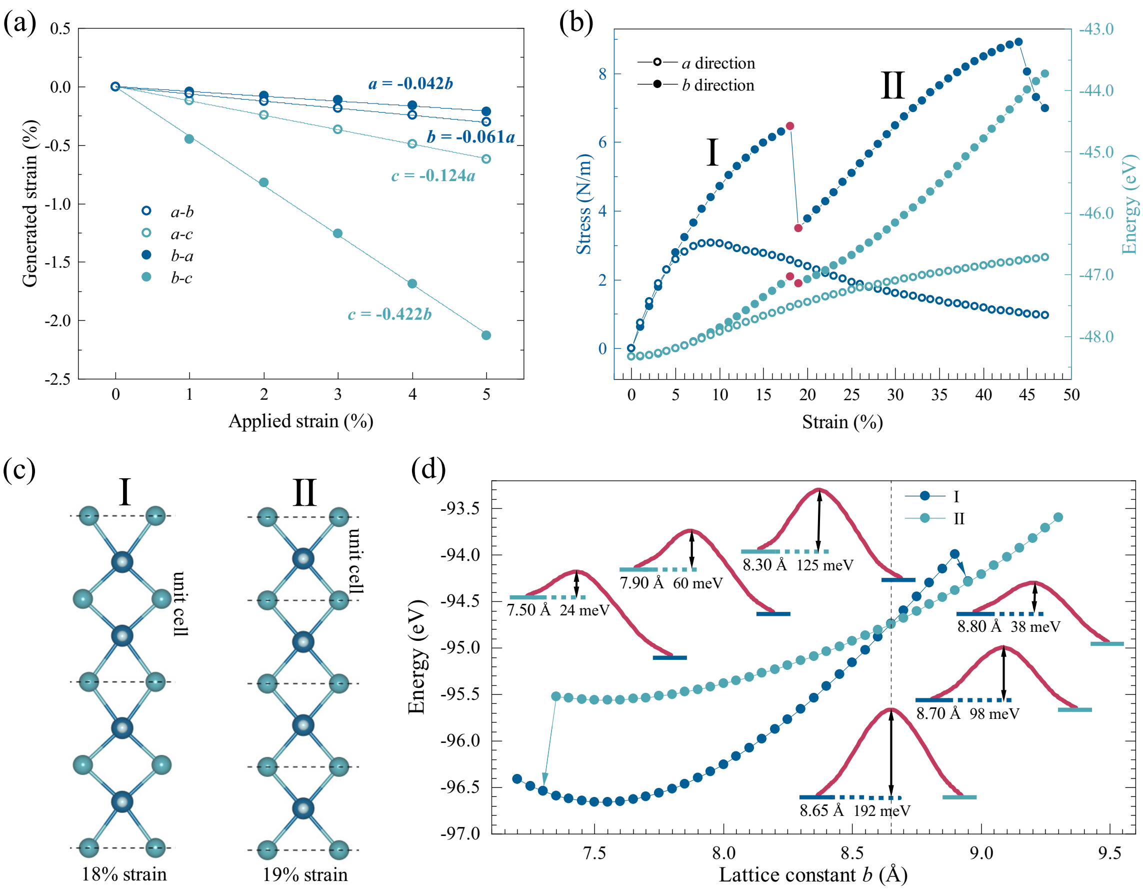

FIG. 2. (a) The applied strain and the generated strain along different directions in the monolayer $NbOI_2$. Data are fitted to function $y = -\upsilon x$ with υ as the linear Poisson's ratio. (b) The stress and energy of the monolayer $NbOI_2$ under uniaxial stretching along the a and b directions. (c) The crystal structure of Phase I and II under strain. (d) Energy of the two phases versus lattice constant b, and schematic diagrams of the barrier (meV/f.u.) for transition with several different b.

determine the Poisson's ratio, as shown in Fig. 2(a). The in-plane Poisson's ratios in the a and b directions are 0.061 and 0.042, respectively. These values are much lower than those of common 2D materials such as graphene [39], and MoS_2 [38], indicating that the strain in one direction has a minimal effect on the other direction. The out-of-plane Poisson's ratios in the a and b directions are 0.124 and 0.422, respectively, demonstrating significant anisotropy.

When applying uniaxial tensile strain in the a direction, it was observed that the maximum stress value of 3.08 $\mathrm{N\,m^{-1}}$ is reached at 9% strain, and gradually decreases afterward, as shown in Fig. 2(b). In the b direction, a notable stress and energy shift occurs at 19% strain. The stress undergoes a release after an initial increase and then rises again with continued application of strain. This abrupt change corresponds to a structural phase transition, as illustrated in Fig. 2(c). At strains of 19% and beyond, the two Nb atoms in the unit cell are no longer dimerization, leading to a higher level of symmetry. We designated this new phase as Phase II, while the initial phase is referred to as Phase I to distinguish between them. Due to the special rhombic grid structure (Fig. S2a within the SM [23]), significant changes occur in bond angles during tension, while bond lengths change little. Under 19% tensile strain, the maximum change in bond length does not exceed 5% (Fig. S2b within the SM [23]). This indicates that the phase transition is experimentally feasible, for example, through the use of elastic substrate materials.

The energy variations of Phases I and II are calculated with respect to their lattice constant in the b direction. The lattice was fully relaxed in the direction perpendicular to the strain. As shown in Fig. 2(d), the energy of both phases increases as a quadratic function of the lattice constant, following typical elastic deformation patterns. When the lattice constant b is less than 8.65 Å, the energy of Phase I is lower than that of Phase II. At $b = 8.65$ Å, where the energy of Phase I and II become equal, a phase transition barrier of 192 meV/f.u. is obtained using the CI-NEB method [31]. We calculated the barriers for different lattice constants, and the trend reveals that when compressing the lattice, the barrier from Phase II to Phase I gradually decreases until it disappears when $b < 7.35$ Å, leading to the absence of Phase II. Conversely, when stretching the lattice, the barrier from Phase I to Phase II decreases until it disappears when $b > 8.90$ Å, resulting in the absence of Phase I. The presence of these barriers allows for the coexistence of both phases within a considerable range of strains. Energy barrier fitting curves with several special constant lattices obtained through NEB calculations can be found in the SM [23].

The ferroelectric properties of monolayer $NbOI_2$ are attributed to the polarization displacement of Nb atoms [14].

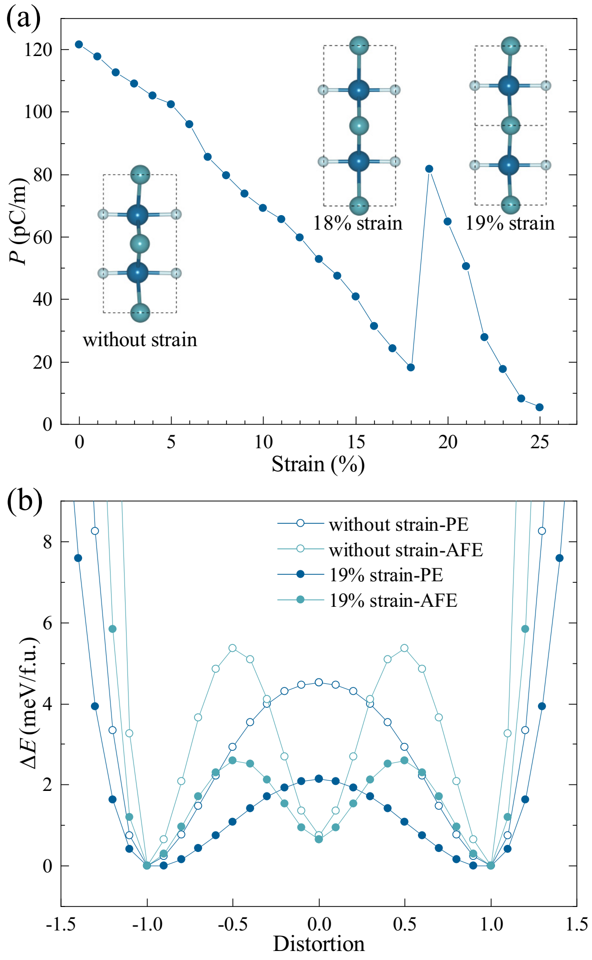

FIG. 3. (a) Calculated polarization of the monolayer $NbOI_2$ under uniaxial stretching along the b direction. The insets are crystal structures under several special strains. (b) Calculated energy walls of FE switching paths through the PE and AFE phases. The data with and without strain are represented by dots and circles, respectively. The zero point of distortion corresponds to the position of Nb atoms in the paraelectric phase, and the negative and positive values indicate the leftward and rightward displacements.

Different combinations of displacement directions for the adjacent Nb atoms correspond to distinct phases. In the paraelectric phase (PE), the Nb atoms show no polarization displacement; in the ferroelectric phase (FE), they exhibit displacements in the same direction; and in the antiferroelectric phase (AFE), the adjacent Nb atoms undergo displacement in opposite directions. Crystal structures of these three phases are shown in Fig. S4 within the SM [23], in which the ferroelectric phase is the ground state. We observed that applying uniaxial strain along the b direction also induces alterations in the polarization displacements. As depicted in Fig. 3(a), Nb atoms gradually approach a higher symmetric position as the strain increases. Therefore, the polarization intensity decreases progressively compared to the ferroelectric polarization value of 121.47 pC/m in the initial structure [40]. However, when the strain reaches 18%, the polarization intensity of the monolayer $NbOI_2$ diminishes to 18.09 pC/m, and the displacement of Nb atoms approaches the paraelectric phase (PE). Upon reaching 19% strain, the transition from Phase I to Phase II leads to a renewed increase in Nb atom displacement, consequently causing the polarization intensity to rise again to 81.64 pC/m. Subsequently, it decreases with further strain.

TABLE II. The calculated lattice constants (Å), energy difference (meV/f.u.), and local magnetic moment on Nb atom (μ_B) of different magnetic configurations in the monolayer $NbOI_2$.

	Lattice constants (a/b)	Energy difference	Magnetic moment
FM	3.92/4.11	153.1	0.78
AFMa	3.92/4.11	153.4	0.76
AFMb	3.92/3.76	1.0	0.45
AFMab	3.92/3.76	0	0.44

Under the influence of an external electric field, the FE polarization direction in monolayer $NbOI_2$ is switchable. The transition may follow two different paths: one through AFE phase and the other through PE phase. The schematic diagrams of crystal structure corresponding to different switching paths can be found in Fig. S5 within the SM [23]. As illustrated in Fig. 3(b), the path via PE phase exhibits a lower barrier, measuring 4.52 meV/f.u. We also computed the reversal barrier under 19% strain, where Phase II appears. Similarly, the PE path has a lower barrier compared to the AFE path. However, the FE reversal barriers for both paths decrease to 2.14 and 2.59 meV/f.u., respectively. This represents a reduction of more than 50% compared to unstrained Phase I, indicating that the phase transition point enables easier realization of ferroelectric switching while maintaining a large polarization value.

Different from Phase I, the monolayer $NbOI_2$ in Phase II shows net magnetic moments on Nb atoms. To verify the magnetic coupling configuration, the ferromagnetic state (FM) and three antiferromagnetic states (AFMa, AFMb, AFMab), as shown in Fig. 4(a), were considered in our calculations. We performed structural optimization for each magnetic configuration and compared their lowest energies to obtain the most stable configuration. During this process, the lattice constants are fully relaxed. The results displayed in Table II reveal that the AFMab state has the lowest energy, where neighboring moments in two orthogonal directions are both arranged antiparallelly. The band structure in Fig. 4(b) indicates that the monolayer $NbOI_2$ in Phase II is an antiferromagnetic semiconductor with an indirect band gap of 1.63 eV. The CBM is located at the Γ point, primarily composed of Nb-$d_{xz/yz}$ orbitals, while the VBM is situated between the S and Y points, dominated by Nb-d_{xy} orbitals. In addition, the increased symmetry eliminates the Nb atom dimerization, preserving the magnetic moments on each Nb^{4+} ion. In comparison to Phase I, the reduction in the localization of electron distribution in the b direction leads to an increased slope of the bands in the X-S and Y-Γ segments. This results in the lowering of the energy of the d_{xy} orbital below the Fermi level, which is occupied by the remaining valence electron of Nb^{4+}. The weaker overlap of adjacent Nb-d_{xy} wave functions, as depicted in Fig. 4(c), prevents the formation of bonding and antibonding

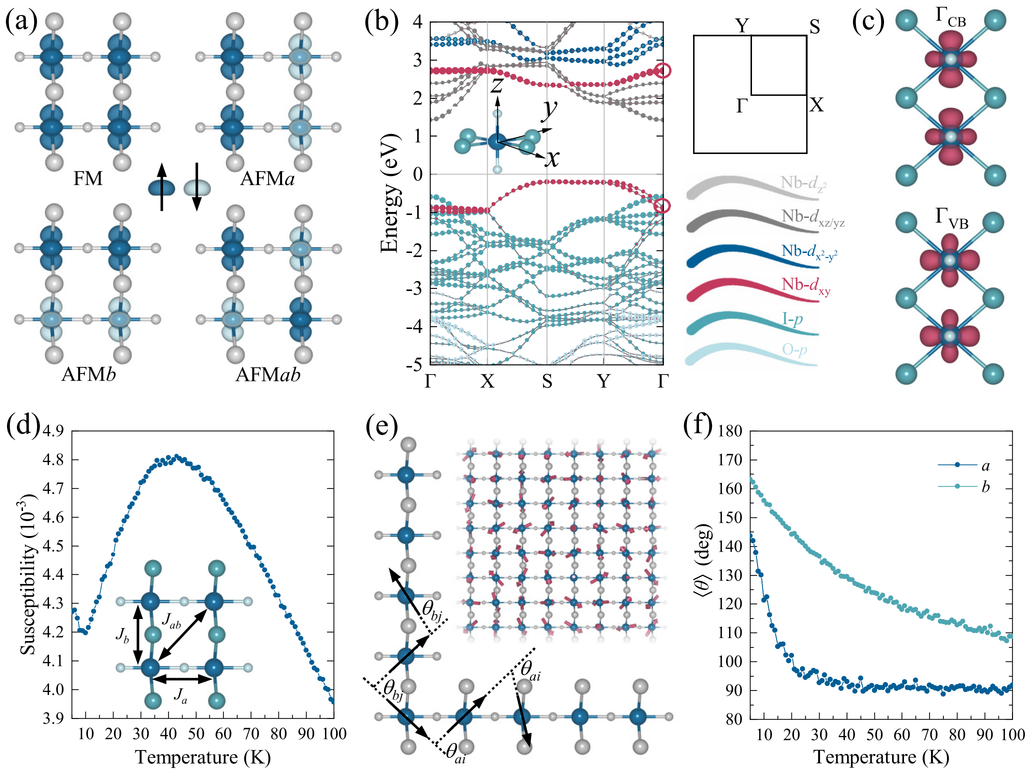

FIG. 4. (a) The spin density of four magnetic orders for the monolayer $NbOI_2$ in Phase II. The isosurface value is 0.01 e/Å^3. (b) Orbital-projected band structure of the AFM*ab* configuration calculated using the HSE06 functional. The inset shows the Cartesian coordinates used in the band calculation. (c) The electron density at Γ points of the band Nb-d_{xy}. The value of the isosurface is 0.005 e/Å^3. (d) The simulated susceptibility as a function of temperature for the monolayer $NbOI_2$. The inset is schematic of the exchange interaction. (e) Schematics to count the spin angle along the *a* and *b* directions in every Monte Carlo step. (f) Calculated $\langle\theta\rangle$ along the *a* and *b* directions for temperature.

states observed in Phase I. The emergence of local magnetism on the Nb atoms is corresponding to the further splitting of the Nb-*d* orbitals, as indicated by the two red lines in Fig. 4(b). The analysis of Brillouin zone folding of the supercell and band splitting in the II phase can be found in the SM [23].

Magnetic anisotropy plays a crucial role in stabilizing the long-range magnetic order of two-dimensional materials [41]. Based on the symmetry, we calculated the magnetic anisotropy energy (MAE) along three crystallographic directions. The results indicate that the easy magnetic axis aligns along the *a* direction (*z* axis), with energy lower by 0.14 meV/f.u. and 0.06 meV/f.u. compared to the *b* and *c* directions, respectively. Using the Heisenberg model, we calculated the nearest-neighbor exchange coefficients J_a and J_b, as well as the next-nearest-neighbor exchange coefficient J_{ab}, based on the energy differences between the FM and AFM magnetic configurations. The Hamiltonian is expressed using formula

$$H = -\sum_{i\neq j} J_{ij}\boldsymbol{S}_i\cdot\boldsymbol{S}_j - \sum_i \left[A_a\left(S_i^a\right)^2 + A_c\left(S_i^c\right)^2\right] \qquad (2)$$

where $\boldsymbol{S}_i$ is the normalized spin ($|\boldsymbol{S}| = 1$) and $A_{a/c}$ is the anisotropy energy parameter. With the same lattice constant, the calculated exchange coefficients are $J_a = -0.32$ meV, $J_b = -30.33$ meV, and $J_{ab} = 0.20$ meV. These results indicate that the interaction coefficient along the *b* direction is significantly greater than that in the *a* direction, consistent with the above analysis of the spatial distribution of Nb-d_{xy} orbital. The negative value indicates a strong antiferromagnetic coupling characteristic, corresponding to the superexchange between Nb^{4+} cations realized via Nb-I hybridization.

Based on the Hamiltonian in Eq. (2), we conducted Monte Carlo simulations of the magnetic order on temperature and predicted the Néel temperature (T_N) of the monolayer $NbOI_2$. Simulations involved a 50 × 50 supercell to model the random spin flips at different temperatures. As shown in Fig. 4(d), the magnetic susceptibility peaks at a T_N of 43 K. It is comparable to the Curie temperature of monolayer CrI_3 [34,42]. It is noted that there is another extremum at temperatures below 10 K. This is attributed to the significant difference in the magnetic coupling strengths between the *a* and *b* directions and the relatively small coupling strength of the next-nearest neighbors. To demonstrate this, we constructed the model shown in Fig. 4(e), defining the angles between adjacent magnetic moments in the *a* and *b* directions as θ_{ai} and θ_{bj}, respectively. By calculating the statistical average of the angles θ_a and θ_b in each Monte Carlo step, we plotted their dependence on temperature in Fig. 4(f). The arrangement of magnetic moments in the two directions exhibits a significant difference with increasing temperature. In the *a* direction, the angle decreases rapidly as temperature increases, quickly reaching a disordered state ($\langle\theta_a\rangle = 90^\circ$). In the *b* direction, the angle decreases more slowly, maintaining antiferromagnetic order to a higher temperature. This stepwise magnetic ordering in 2D materials could play a crucial role in future high-performance micro devices such as storage, sensors, and information technologies. In addition, recent research has proposed a mechanism named EPDQ to utilize electric fields for switching magnetic topological charges in monolayer VOI_2 [43]. This is also possible to achieve in the $NbOI_2$, which has a ferroelectric and magnetic ordering similar to VOI_2.

IV. CONCLUSIONS

In summary, we conducted first-principles calculations to investigate the structural and physical characteristics of monolayer $NbOI_2$ under tensile strain. Our calculations revealed that the material has a low Young's modulus and a small Poisson's ratio, making monolayer $NbOI_2$ easily tunable under mechanical stress. Uniaxial stress in the *b* direction induces a structural phase transition, followed by a magnetic phase transition from NM to AFM state. The strain also reduces the barrier for switching its FE polarization direction by over 50%. Additionally, we observed a pronounced anisotropy in the arrangement of magnetic moments against temperature, leading to an intriguing stepwise magnetic ordering phenomenon. The predictions and analyses of the strain characteristics of monolayer $NbOI_2$ in this study provide valuable insights into utilizing this 2D material in future flexible microdevices. Furthermore, these findings also contribute to a deeper understanding of phase transitions in 2D materials.

ACKNOWLEDGMENTS

This work is supported by the National Key Research and Development Program of China (Grants No. 2023ZD0120700, No. 2022YFB3807200, No. 2022YFA1503103), Natural Science Foundation of China (Grants No. T2321002, No. 21973011, No. 22033002, No. 92261112), the Postgraduate Research & Practice Innovation Program of Jiangsu Province (Grant No. KYCX23_0223), Natural Science Foundation of Jiangsu Province, Major Project (Grant No. BK20232012). The authors thank the computational resources from the Big Data Computing Center of SEU.

---

[1] Q. B. Zhu, B. Li, D. D. Yang, C. Liu, S. Feng, M. L. Chen, Y. Sun, Y. N. Tian, X. Su, X. M. Wang *et al.*, A flexible ultrasensitive optoelectronic sensor array for neuromorphic vision systems, Nat. Commun. **12**, 1798 (2021).

[2] H. Hu, H. Huang, M. Li, X. Gao, L. Yin, R. Qi, R. S. Wu, X. Chen, Y. Ma, K. Shi *et al.*, A wearable cardiac ultrasound imager, Nature (London) **613**, 667 (2023).

[3] Q. Yang, W. Jin, Q. Zhang, Y. Wei, Z. Guo, X. Li, Y. Yang, Q. Luo, H. Tian, and T.-L. Ren, Mixed-modality speech recognition and interaction using a wearable artificial throat, Nat. Mach. Intell **5**, 169 (2023).

[4] J. Qiao, X. Kong, Z. X. Hu, F. Yang, and W. Ji, High-mobility transport anisotropy and linear dichroism in few-layer black phosphorus, Nat. Commun. **5**, 4475 (2014).

[5] Y. Liu, A. Elbanna, W. Gao, J. Pan, Z. Shen, and J. Teng, Interlayer excitons in transition metal dichalcogenide semiconductors for 2D optoelectronics, Adv. Mater. **34**, 2107138 (2022).

[6] R. Peng, A. Ripin, Y. Ye, J. Zhu, C. Wu, S. Lee, H. Li, T. Taniguchi, K. Watanabe, T. Cao *et al.*, Long-range transport of 2D excitons with acoustic waves, Nat. Commun. **13**, 1334 (2022).

[7] K. S. Burch, D. Mandrus, and J. G. Park, Magnetism in two-dimensional van der Waals materials, Nature (London) **563**, 47 (2018).

[8] Q. Chen, R. Wang, Z. Huang, S. Yuan, H. Wang, L. Ma, and J. Wang, Two dimensional $CrGa_2Se_4$: A spin-gapless ferromagnetic semiconductor with inclined uniaxial anisotropy, Nanoscale **13**, 6024 (2021).

[9] W. Ding, J. Zeng, W. Qin, P. Cui, and Z. Zhang, Exploring high transition temperature superconductivity in a freestanding or $SrTiO_3$-supported CoSb monolayer, Phys. Rev. Lett. **124**, 027002 (2020).

[10] P. Johari and V. B. Shenoy, Tuning the electronic properties of semiconducting transition metal dichalcogenides by applying mechanical strains, ACS Nano **6**, 5449 (2012).

[11] J. Feng, X. Qian, C.-W. Huang, and J. Li, Strain-engineered artificial atom as a broad-spectrum solar energy funnel, Nat. Photonics **6**, 866 (2012).

[12] S. Yang, C. Wang, H. Sahin, H. Chen, Y. Li, S. S. Li, A. Suslu, F. M. Peeters, Q. Liu, J. Li, and S. Tongay, Tuning the optical, magnetic, and electrical properties of $ReSe_2$ by nanoscale strain engineering, Nano Lett. **15**, 1660 (2015).

[13] G. Zhang, K. Lu, Y. Wang, H. Wang, and Q. Chen, Mechanical and electronic properties of α-M_2X_3 (M = Ga, In; X = S, Se) monolayers, Phys. Rev. B **105**, 235303 (2022).

[14] Y. Jia, M. Zhao, G. Gou, X. C. Zeng, and J. Li, Niobium oxide dihalides $NbOX_2$: A new family of two-dimensional van der Waals layered materials with intrinsic ferroelectricity and antiferroelectricity, Nanoscale Horizons **4**, 1113 (2019).

[15] Y. Fang, F. Wang, R. Wang, T. Zhai, and F. Huang, 2D $NbOI_2$: A chiral semiconductor with highly in-plane anisotropic electrical and optical properties, Adv. Mater. **33**, 2101505 (2021).

[16] L. Ye, W. Zhou, D. Huang, X. Jiang, Q. Guo, X. Cao, S. Yan, X. Wang, D. Jia, D. Jiang, Y. Wang *et al.*, Manipulation of nonlinear optical responses in layered ferroelectric niobium oxide dihalides, Nat. Commun. **14**, 5911 (2023).

[17] J. Fu, N. Yang, Y. Liu, Q. Liu, J. Du, Y. Fang, J. Wang, B. Gao, C. Xu, D. Zhang *et al.*, Emission dipole and pressure-driven tunability of second harmonic generation in vdWs ferroelectric $NbOI_2$, Adv. Funct. Mater. **34**, 2308207 (2023).

[18] I. Abdelwahab, B. Tilmann, Y. Wu, D. Giovanni, I. Verzhbitskiy, M. Zhu, R. Berté, F. Xuan, L. d. S. Menezes, G. Eda *et al.*, Giant second-harmonic generation in ferroelectric $NbOI_2$, Nat. Photonics **16**, 644 (2022).

[19] Y. Wu, I. Abdelwahab, K. C. Kwon, I. Verzhbitskiy, L. Wang, W. H. Liew, K. Yao, G. Eda, K. P. Loh, L. Shen, and S. Y. Quek, Data-driven discovery of high performance layered van der Waals piezoelectric $NbOI_2$, Nat. Commun. **13**, 1884 (2022).

[20] Y. Cui, S. Li, X. Zhang, T. Wang, X. Cao, S. Yan, X. Zhang, H. Lei, G. Tang, J. Hong, and X. Wang, In-plane anisotropic

mechanical properties of two-dimensional $NbOI_2$, Appl. Phys. Lett. **123**, 051905 (2023).

[21] G. Kresse and J. Furthmuller, Efficient iterative schemes for *ab initio* total-energy calculations using a plane-wave basis set, Phys. Rev. B **54**, 11169 (1996).

[22] J. P. Perdew, K. Burke, and M. Ernzerhof, Generalized gradient approximation made simple, Phys. Rev. Lett. **77**, 3865 (1996).

[23] See Supplemental Material at http://link.aps.org/supplemental/10.1103/PhysRevB.109.184103 for van der Waals correction comparison, alterations of bond angle and bond length under uniaxial stretching along the b direction, NEB barriers between Phase I and II with different lattice constants, crystal structures of monolayer $NbOI_2$ in PE, FE, and AFE polarization phases, schematic diagrams of different switching paths and the analysis of band splitting in Phase II.

[24] S. Grimme, J. Antony, S. Ehrlich, and H. Krieg, A consistent and accurate *ab initio* parametrization of density functional dispersion correction (DFT-D) for the 94 elements H-Pu, J. Chem. Phys. **132**, 154104 (2010).

[25] J. Rijnsdorp and F. Jellinek, The crystal structure of niobium oxide diiodide $NbOI_2$, J. Less-Common Met. **61**, 79 (1978).

[26] J. Heyd, J. E. Peralta, G. E. Scuseria, and R. L. Martin, Energy band gaps and lattice parameters evaluated with the Heyd-Scuseria-Ernzerhof screened hybrid functional, J. Chem. Phys. **123**, 174101 (2005).

[27] T. M. Henderson, J. Paier, and G. E. Scuseria, Accurate treatment of solids with the HSE screened hybrid, Physica Status Solidi (b) **248**, 767 (2011).

[28] S. Steiner, S. Khmelevskyi, M. Marsmann, and G. Kresse, Calculation of the magnetic anisotropy with projected-augmented-wave methodology and the case study of disordered $Fe_{1-x}Co_x$ alloys, Phys. Rev. B **93**, 224425 (2016).

[29] H. J. Monkhorst and J. D. Pack, Special points for Brillouin-zone integrations, Phys. Rev. B **13**, 5188 (1976).

[30] A. Togo, F. Oba, and I. Tanaka, First-principles calculations of the ferroelastic transition between rutile-type and $CaCl_2$-type SiO_2 at high pressures, Phys. Rev. B **78**, 134106 (2008).

[31] G. Henkelman, B. P. Uberuaga, and H. Jónsson, A climbing image nudged elastic band method for finding saddle points and minimum energy paths, J. Chem. Phys. **113**, 9901 (2000).

[32] R. D. King-Smith and D. Vanderbilt, Theory of polarization of crystalline solids, Phys. Rev. B **47**, 1651 (1993).

[33] G. S. Joyce, Classical Heisenberg model, Phys. Rev. **155**, 478 (1967).

[34] Y. Zhang, B. Wang, Y. Guo, Q. Li, and J. Wang, A universal framework for metropolis Monte Carlo simulation of magnetic Curie temperature, Comput. Mater. Sci. **197**, 110638 (2021).

[35] Y. Wang, F. Li, Y. Li, and Z. Chen, Semi-metallic Be_5C_2 monolayer global minimum with quasi-planar pentacoordinate carbons and negative Poisson's ratio, Nat. Commun. **7**, 11488 (2016).

[36] J. H. Kim, J. H. Jeong, N. Kim, R. Joshi, and G.-H. Lee, Mechanical properties of two-dimensional materials and their applications, J. Phys. D **52**, 083001 (2019).

[37] B. Wang, Q. Wu, Y. Zhang, L. Ma, and J. Wang, Auxetic B_4N monolayer: A promising 2D material with in-plane negative Poisson's ratio and large anisotropic mechanics, ACS Appl. Mater. Interfaces **11**, 33231 (2019).

[38] K. Liu, Q. Yan, M. Chen, W. Fan, Y. Sun, J. Suh, D. Fu, S. Lee, J. Zhou, S. Tongay *et al.*, Elastic properties of chemical-vapor-deposited monolayer MoS_2, WS_2, and their bilayer heterostructures, Nano Lett. **14**, 5097 (2014).

[39] C. Lee, X. Wei, J. W. Kysar, and J. Hone, Measurement of the elastic properties and intrinsic strength of monolayer graphene, Science **321**, 385 (2008).

[40] It is equivalent to $16.55\ \mu C/cm^2$ in three dimensions for a layer thickness of 7.34 Å [14].

[41] M. Wang, C. Huang, C. Cheung, C. Chen, S. G. Tan, T. Huang, Y. Zhao, Y. Zhao, G. Wu, Y. Feng *et al.*, Prospects and opportunities of 2D van der Waals magnetic systems, Ann. Phy. **532**, 1900452 (2020).

[42] B. Huang, G. Clark, E. Navarro-Moratalla, D. R. Klein, R. Cheng, K. L. Seyler, D. Zhong, E. Schmidgall, M. A. McGuire, D. H. Cobden *et al.*, Layer-dependent ferromagnetism in a van der Waals crystal down to the monolayer limit, Nature (London) **546**, 270 (2017).

[43] C. Xu, P. Chen, H. Tan, Y. Yang, H. Xiang, and L. Bellaiche, Electric-field switching of magnetic topological charge in type-I multiferroics, Phys. Rev. Lett. **125**, 037203 (2020).